A Pulsed-Coherent Lidar With Sub-10 μm Precision

Li-Yang Chen, *Member, IEEE*, Abhinav Kumar Vinod, James F. McMillan, Hangbo Yang, Chee Wei Wong, *Fellow, IEEE*, and C.-K. Ken Yang, *Fellow, IEEE*

***Abstract*— This article presents a pulsed-coherent lidar that uses a 19-GHz pulse-modulated optical carrier and segmented time-of-flight (ToF) detection. The receiver analog frontend (AFE) employs a down-conversion chain that consists of a phase-invariant programmable-gain low-noise amplifier (PI-PGLNA), a sub-harmonic mixer (SHM), and an inverter-based phase-invariant programmable-gain amplifier (PI-PGA). The local oscillator (LO) is generated from a phase-locked loop (PLL) with a ring-type voltage-controlled oscillator (VCO). An analog-to-digital converter (ADC) subsamples the down-converted signal, and a digital signal processor (DSP) calculates the coarse, intermediate, and fine ToF. At the receiver input, a narrowband matching is implemented between the p-i-n photodiode and the PI-PGLNA with direct wire bonding. The system achieves 6-μm precision with a 5-MSa/s sampling rate at a 2.5-m distance. The 2-D scanning is achieved with this lidar with the use of an MEMS mirror.**

***Index Terms*— Amplitude-modulated continuous-wave (AMCW), coherent, inverter-based, lidar, phase-invariant, programmable gain amplifier, pulsed, time-of-flight (ToF).**

I. Introduction

A LIDAR is a ranging system that uses light as a carrier to measure the distance. It has been widely used in a multitude of applications ranging from atmospheric sensing and meteorology to navigation and topographical mapping. Different specifications in terms of distance, precision, and sampling rate lead to different architectures and implementations. Speed-oriented lidars [1]–[7], which can do fast scanning, are primarily implemented in direct time-of-flight (ToF) detection. Precision-oriented lidars [8]–[14], which can achieve better than sub-millimeter precision, are mainly based on indirect ToF detection.

A pulsed lidar shown in Fig. 1(a) measures the ToF directly. The transmitting laser is modulated to send out a single pulse of light. Upon the transmission, a high-frequency counter starts to count. When the receiver detects the echoed signal, the counter stops, and the resulting count reflects the ToF. The distance (d) can be converted from the ToF (Δt)

$$d = c \times \frac{\Delta t}{2} \tag{1}$$

where c is the speed of light. Although the pulsed lidar can achieve fast acquisition, walk error and the nonlinearity of the time-to-digital converter (TDC) limit the accuracy of the lidar system, whereas clock jitter, aperture jitter, and quantization error limit the precision. Clock jitter and quantization error are noise sources common to any digitizing system. Aperture jitter (σ_j) depends on the implementation of the analog frontend (AFE) and can be further expressed as

$$\sigma_j = \frac{0.35}{\text{SNR} \cdot \text{BW} \cdot \sqrt{N}} \tag{2}$$

where SNR indicates the signal-to-noise ratio at the receiver frontend, BW is the bandwidth of the receiver, and N is the averaging factor of how many pulses are collected for averaging.

For a conventional pulsed lidar with a typical receiver bandwidth smaller than 500 MHz [15]–[17], even with a high SNR of 40 dB, the aperture jitter contributes as much as 7-ps rms of jitter which corresponds to 1-mm precision. One solution to suppress the aperture jitter is to increase the averaging factor (N), but it directly trades off with the acquisition speed. The sampling rate has to drop to one-fourth of the original speed to reduce the aperture jitter by half. Another possible way is to increase the receiver's bandwidth so that the incoming signal has a sharper transition edge. The slope of the transition is inversely proportional to the bandwidth; however, the noise bandwidth also increases proportionally, and SNR drops by a factor of $1/\sqrt{\text{BW}}$. Therefore, increasing the receiver's bandwidth does not directly lead to improved accuracy.

Besides the limited precision, the performance of a pulsed lidar also suffers from walk error. While it is possible to calibrate the delay dependence on the input signal strength with a large lookup table, the table is susceptible to environmental variations that lead to measurement inaccuracies. In [16], a high-pass timing discriminator compensates the dc offset. Designs such as [1], [2], and [17] use a high-pass filter to convert the input pulse to a bipolar pulse and define the crossing point as the arrival time. Dual-threshold detection [3] has also been used to determine the slew rate to then extrapolate the arrival time. Overall, the walk error limits the accuracy to a few millimeters with many such first-order compensation techniques.

One example of indirect ToF measurement is phase detection which has also been referred to as coherent detection.

Manuscript received 14 August 2021; revised 11 January 2022; accepted 23 April 2022. Date of publication 9 May 2022; date of current version 25 July 2022. This article was approved by Associate Editor David Stoppa. *(Corresponding author: Li-Yang Chen.)*

Li-Yang Chen was with the Department of Electrical and Computer Engineering, University of California at Los Angeles, Los Angeles, CA 90095 USA. He is now with AMD/Xilinx, San Jose, CA 95124 USA (e-mail: liyang.chen@amd.com).

Abhinav Kumar Vinod was with the Department of Electrical and Computer Engineering, University of California at Los Angeles, Los Angeles, CA 90095 USA. He is now with Intel, San Jose, CA 95134 USA (e-mail: abhinav.vinod@intel.com).

James F. McMillan, Hangbo Yang, Chee Wei Wong, and C.-K. Ken Yang are with the Department of Electrical and Computer Engineering, University of California at Los Angeles, Los Angeles, CA 90095 USA.

Color versions of one or more figures in this article are available at https://doi.org/10.1109/JSSC.2022.3170909.

Digital Object Identifier 10.1109/JSSC.2022.3170909

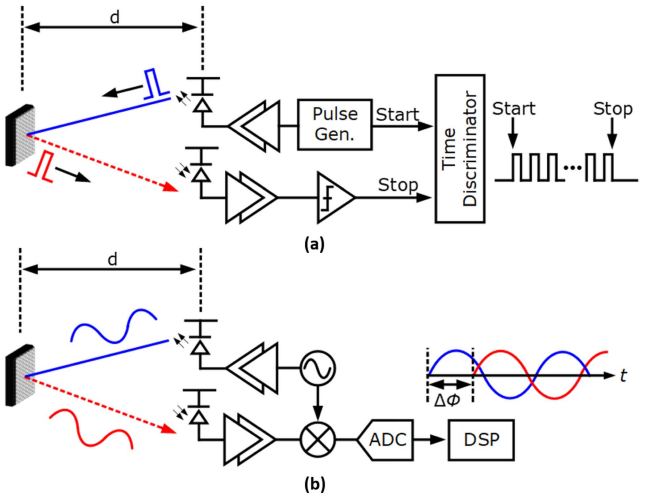

Fig. 1. Architectures of (a) pulsed lidar and (b) phase-based lidar.

The system architecture is shown in Fig. 1(b). The transmitter sends a continuous sine wave at a carrier frequency f_{ref}, and a phase detector then detects the phase shift ($\Delta\phi_{\text{ref}}$) of the received signal. The measured distance (d) can be calculated as

$$d = c \times \frac{(\Delta\phi_{\text{ref}}/2\pi) \times T_{\text{ref}}}{2} \tag{3}$$

where T_{ref} is the period of the carrier, $1/f_{\text{ref}}$. The phase detection can be performed either optically which is known as interferometry [11], [12], [18]–[23], or electrically with an amplitude-modulated continuous-wave (AMCW) signal [9], [10], [24]–[26]. When compared to the pulsed lidar, the aperture jitter in phase detection can be expressed as

$$\sigma_j = \frac{1}{2\pi f_{\text{ref}} \cdot \text{SNR}} \tag{4}$$

which shows that the slope of the signal at the zero-crossing point can be decoupled from the receiver's bandwidth with a narrowband filter. Therefore, a phase lidar can achieve higher precision by shifting the carrier to higher frequency with a constant bandwidth. Furthermore, the walk error is suppressed since the dc component can be easily removed by ac-coupling.

The main challenge of a phase-detection lidar is aliasing. Since the transmitted signal is periodic, the receiver cannot distinguish the difference beyond one carrier period. A common solution to extend the measurable distance is with segmented measurements. In [8] and [9], two laser sources at different wavelengths are modulated separately by electrooptic modulators (EOMs); one at a high frequency and another one at a low frequency. The low frequency of modulation measures the full range of distance and quantizes the ToF into a number of cycles of the high modulation frequency. Finer precision is then measured within a period of the high modulation frequency. While this segmented detection extends the measurable distance, the system doubles the power consumption. Also, to meet the safety regulation, the peak power is reduced since the transmitter emits two laser carriers simultaneously, hence limiting the reachable distance. Lastly, the receiver requires two separate paths in the coarse and fine measurements which would then require alignment that is sensitive to variations and mismatch.

The potential of a high sampling rate and high precision system enables their usage in new applications requiring mapping of complex environments with high frame rates, which is of particular relevance to biometric securities, autonomous vehicles, indoor robotics, and topographical mapping via drones. In addition, it would also find applications in sensors for next-generation augmented reality on mobile platforms. In this work, our design goal is to develop a lidar system that can achieve high precision ($<$10 μm) while keeping the fast scanning speed ($>$1 MHz).

This article is organized as follows. Section II discusses the system consideration including the detection algorithm, noise limitation, and the frequency planning of the segmented detection. Section III presents the receiver's design using a narrowband matching, a phase-invariant AFE, and a local oscillator (LO) with low phase noise. Section IV shows the measurement results of the building blocks and the system operation, and Section V summarizes this work.

II. Pulsed-Coherent Detection

A. Detection Algorithm

The idea of pulsed-coherent detection is to combine the advantages of both direct ToF detection and phase detection. The pulsed envelope modulation enables high-speed acquisition, and the coherent phase-detection provides high precision. A CW laser source is amplitude modulated by both a high RF carrier (f_{ref}) and a low-frequency pulsed envelope modulation (f_m). To find the ToF, the coarse detection is measured by counting the arrival time of the pulse envelope, and the fine detection is by measuring the phase shift of the RF carrier. The pulsed-coherent detection not only has a better precision-speed tradeoff, but also simplifies the optical setup. Compared to AMCW lidar which uses two laser carriers and two receiving channels, the pulsed-coherent detection only requires a single laser source and a single-channel receiver. Also, the measurable distance can be further extended by increasing optical power and adding more registers to the coarse counter.

Instead of transmitting a single pulsed envelope, the sequence can be encoded with multiple pulses and averaged for higher precision. Fig. 2(a) shows an example of the encoded waveform. The carrier is modulated by a 1010... pattern followed by a long run of zeros. The deadtime (T_{dz}) is a blank period to prevent multiple reflections. The system design can be flexibly adjusted based on various application requirements. We design our system to be segmented and allow for a change of parameters in an onboard digital signal processor (DSP) to optimize the range, precision, and SNR tradeoff as per the requirement. For the applications that require high precision, the encoded transmission sequence can be extended to increase the integration time and gather more energy from the target, thus improving the accuracy and the measurement distance. For fast acquisition applications, a shorter transmission format can accelerate the sampling speed. This flexibility helps the ranging in a dynamical and complex environment.

At the receiving end, the overall ToF (ToF_{all}) is partitioned into three segments as shown in Fig. 2(b). The detection of

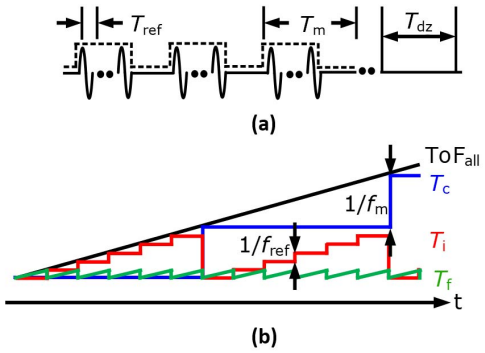

Fig. 2. Pulsed-coherent lidar (a) transmission format and (b) detection algorithm.

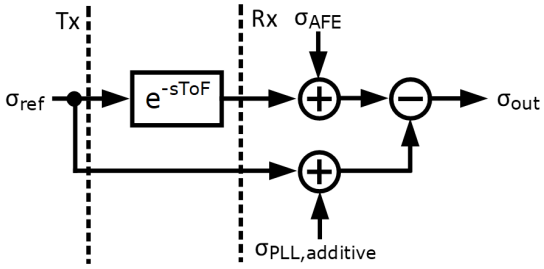

Fig. 3. Simplified noise model of the coherent detection.

the coarse segment (T_c) is counting the ToF at the envelop modulation rate (f_m). To detect the arrival time within a modulation period, the intermediate segment (T_i) counts at a rate of the carrier frequency (f_{ref}) the number of cycles. To detect the fine segment (T_f), the phase shift within a carrier's period ($1/f_{\text{ref}}$) is measured. The overall ToF is expressed as

$$\text{ToF}_{\text{all}} = N_1 \frac{1}{f_m} + N_2 \frac{1}{f_{\text{ref}}} + \frac{\phi_{\text{ref}}}{360^\circ} \frac{1}{f_{\text{ref}}} \tag{5}$$

where N_1 and N_2 are the counts of the counters, and ϕ_{ref} is the phase shift of the RF carrier. With sufficient sensitivity of the front-end, the acquisition range can be linearly increased by simply adding more bits to the counter.

B. Noise Analysis

To estimate the system's precision, we use a simplified noise model of the coherent detection, as shown in Fig. 3, which illustrates the dominant noise sources. The main noise sources are from the reference clock for the phase detection (σ_{clk}), and from the receiver's AFE (σ_{AFE}) including the shot noise of the photodiode and the thermal noise from both the photodiode and the analog AFE.

1) Clock Noise: The clock noise, σ_{clk}, includes correlated and uncorrelated noise. The phase noise of the reference clock, σ_{ref}, is a correlated noise source since it is used to synchronize both the transmitter and the receiver. The uncorrelated noise is primarily from the additive noise from the LO generation, which is typically from a phase-locked loop (PLL), $\sigma_{\text{PLL,additive}}$.

The ToF delay can be represented as $e^{-\text{sToF}}$ in the s-domain. A phase detector compares the phase to the reference by down-converting the carrier to the sampling rate. The output noise of the correlated noise can then be modeled as

$$\sigma^2_{\text{out,ref}} = \sigma^2_{\text{ref}} \times \left|1 - e^{-\text{sToF}}\right|^2 \tag{6}$$

which shows a high-pass response due to the noise filtering. Fig. 4(a) shows the phase noise of the reference filtered by different ToFs ranging from 1 to 1000 ns which correspond to 0.15–150 m in distance.

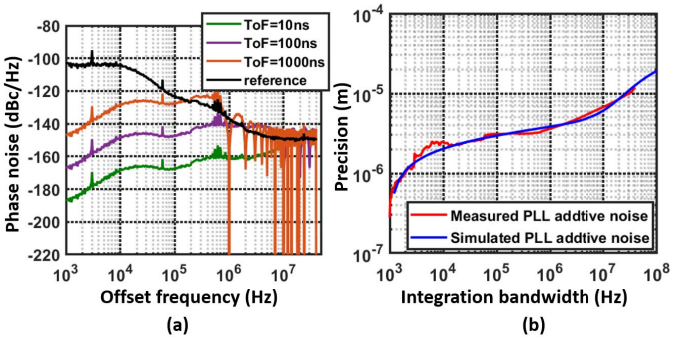

Fig. 4. Clock noise. (a) Correlated noise. (b) Uncorrelated noise.

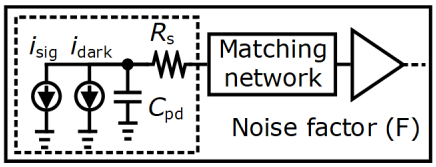

Fig. 5. Noise model of the AFE.

The noise characteristic of the LO generation varies between architectures. This analysis assumes that the LO generation is a conventional PLL. The main sources of noise are the charge pump (CP) and the voltage-controlled oscillator (VCO). Fig. 4(b) shows the additive noise from the PLL with different integration bandwidths from 1-kHz frequency offset. The in-band noise is primarily contributed by the CP where the VCO's phase noise is the dominant out-of-band noise source.

2) AFE Noise: Fig. 5 shows the noise model of the AFE. The diode's model consists of the signal's current (i_{sig}), dark current (i_{dark}), and parasitic resistance (R_s) and capacitance (C_{pd}). A matching network performs the impedance matching of the photodiode and the AFE circuit with a noise factor of F. The AFE noise is expressed as

$$\sigma_{\text{AFE}} = \frac{1}{2\pi f_{\text{ref}} \text{SNR}} \tag{7}$$

where the signal-to-noise ratio is

$$\text{SNR} = \sqrt{\frac{i^2_{\text{sig}}}{i^2_{n,\text{in}} \times \text{BW}}}. \tag{8}$$

$i_{n,\text{in}}$ is the total input-referred noise which includes three parts.

1) The shot noise of the photodiode from the dark current, expressed as $i_{s,d}$ in the equation

$$i^2_{s,d} = 2q i_{\text{dark}}. \tag{9}$$

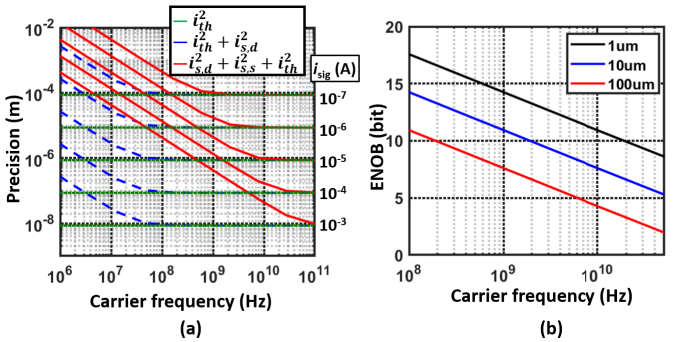

Fig. 6. (a) Precision with different carrier frequencies and input signal powers and (b) ENOB requirement of the phase detector.

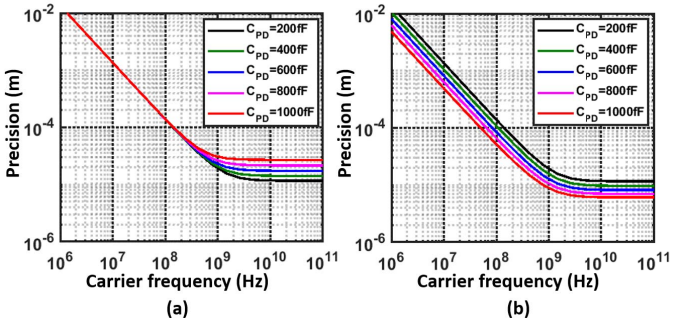

Fig. 7. Noise in different optical setups. (a) Signal power is independent to the photodiode's aperture. (b) Signal power depends on the photodiode's aperture.

2) The shot noise from the signal current, expressed as $i_{s,s}$ in the equation

$$i_{s,s}^2 = 2qi_{\text{sig}}. \tag{10}$$

where q is the electric charge.

3) The thermal noise from the photodiode's parasitic resistance and the noise from the amplifiers. With a narrowband matching network, the analysis in [27]–[29] indicates that the thermal noise current, i_{th}, can be expressed as

$$i_{\text{th}}^2 = 4KT\left(2\pi f_{\text{ref}} C_{\text{pd}}\right)^2 R_s F \tag{11}$$

where K is Boltzmann's constant, and T is the temperature in Kelvin.

The concept of the narrowband optical receiver has been widely used in radio-in-fiber (RFoF) communication [30]–[34] but has not been utilized in lidar to improve the noise performance. Combining (7)–(11), we obtain an overall total noise equation for the AFE

$$\sigma_{\text{AFE}}^2 = \frac{1}{4\pi^2}\frac{\text{BW}}{i_{\text{sig}}^2}\frac{i_{n,\text{in}}^2}{f_{\text{ref}}^2} \tag{12}$$

where the noise current is

$$i_{n,\text{in}}^2 = i_{s,d}^2 + i_{s,s}^2 + i_{\text{th}}^2. \tag{13}$$

Fig. 6(a) shows the precision considering the AFE's noise versus the carrier frequency (f_{ref}) with the received current swept from 100 nA to 1 mA. Here, we assume that the noise factor of the receiver frontend is 2, the parasitic resistance of the photodiode is 10 Ω, parasitic capacitance is 100 fF, dark current is 400 pA, and the integration bandwidth is 1 MHz. At a high carrier frequency, the noise floor is limited by the thermal noise and the clock jitter. At lower carrier frequencies, the shot noise kicks in and limits the precision. It is worthwhile to note that the noise floor is independent of the carrier frequency at high carrier frequencies.

C. Carrier Frequency Selection

The modulation frequencies, f_{ref} and f_m, are chosen based on three factors: noise, the accuracy of the phase detector, and the optical system. From the noise analysis in Section II-B and to achieve better than 10-μm precision, the clock jitter should be <66 fs within the integration bandwidth and the carrier frequency >10 GHz so that the precision is only limited by the thermal noise and the clock jitter. The second consideration is the accuracy of the phase detector. Fig. 6(b) shows the tradeoff between the effective number of bits (ENOB) of the analog-to-digital converter (ADC) and the carrier frequency. By using a carrier frequency higher than 10 GHz, an efficient ADC with a reasonable ENOB of 7–8 bit can be used to achieve our target precision of 10 μm.

So far, the analysis has only considered the limitation of the electrical system. Note that the input signal power is determined by the optical setup of the receiver, particularly the receiver frontend's focal lens. Different optical setups would lead to different choices of photodiodes. In a best-case scenario, assuming that the lens can focus the light to an area smaller than the photodiode, the input power is then constant regardless of the area of the photodiode. According to (12), the AFE noise is proportional to the size of the photodiode, A_{pd}, since

$$\sigma_{\text{AFE}}^2 \propto \frac{C_{\text{pd}}^2 R_s}{i_{\text{sig}}^2} \tag{14}$$

where $C_{\text{pd}} \propto A_{pd}$ and $R_s \propto 1/A_{\text{pd}}$. Therefore, a smaller photodiode is desired to minimize the AFE noise. The simulation results are shown in Fig. 7(a). At high carrier frequency, the noise floor shifts lower with a smaller photodiode.

In a more realistic scenario, because beam divergence trades off with the depth-of-the-view and the angle-of-view, for any application that requires a wide dynamic range of the depth-of-the-view, the beamwidth of the returned signal is commonly larger than the diameter of the photodiode. This is especially the case for the high-speed p-i-n photodiode which has a small aperture. In addition to the high carrier frequency, a larger active area is then desired since the signal current (i_{sig}) is increased with a larger aperture. Fig. 7(b) shows the simulation results where the input power is proportional to the active area of the photodiode. This scenario highlights another advantage of the narrowband pulsed-coherent lidar over the broadband design. For the conventional pulsed lidar with a broadband termination, the bandwidth limits the size of the photodiode by the RC time constant. In contrast, a pulsed-coherent lidar provides the flexibility of the photodiode's selection to

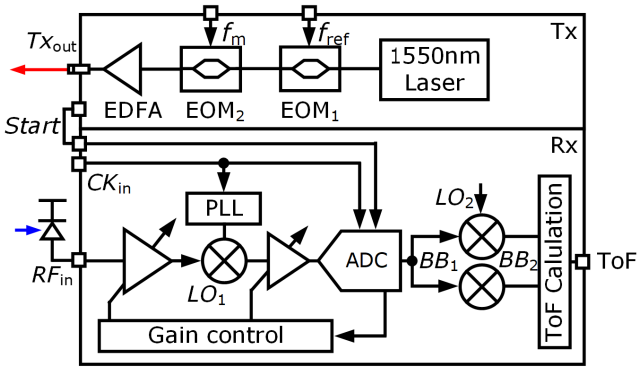

Fig. 8. Essential building blocks of the pulsed-coherent lidar.

optimize the noise performance since we can customize the matching network according to the different photodiodes.

It is worth noting that choosing a high carrier frequency has the benefit of enabling chip-scale integration of an ultralow phase noise light source. A chip-scale frequency comb that has been demonstrated to purify phase noise for pulses at 10's of GHz can be integrated to generate the reference clock [35]–[39]. Moreover, the multiple spectral comb teeth is usable for parallel scanning which can further improve the sampling rate [40], [41].

In the final system, targeting 10 μm of precision, we design the RF carrier at 19 GHz which balances noise and ENOB tradeoff. The design further provides the ability to integrate with a chip-scale micro-comb. The low-frequency envelope modulation is designed at 148 MHz ($1/128 f_{\text{ref}}$) so that the low-frequency modulation provides 8–9 bits of dynamic range. For the precision of the low-frequency modulation, the last two significant bits overlap with the fine detection to manage the handover between the segments.

D. System Architecture

The fundamental building blocks of the pulsed-coherent lidar are shown in Fig. 8. On the transmit side, a laser with a wavelength of 1550 nm is used and the output is modulated with a cascade of two EOMs to perform both RF modulation and envelope modulation. The first EOM is modulated by the RF carrier (f_{ref}), and a pulse-generator modulates the second EOM at a lower rate of f_m. An erbium-doped fiber amplifier (EDFA) then amplifies and sends out the amplitude-modulated signal. To synchronize the transmitter and the receiver, the same pulse sequence is also used as a timestamp. It is embedded in the last significant bit of the ADC, acting as a reference starting point for the ToF calculation.

Instead of finding the coarse ToF and the fine ToF as two separate paths [42], a DSP-based receiver performs the detection of both [43]. An ADC samples the IF signal, and a DSP post-processes the segmented ToF in the digital domain. The pulsed modulation is oversampled by the ADC and hence can be reconstructed in the digital domain. This DSP-based receiver improves the sensitivity to PVT variation. It inherently aligns the segmented measurements using the sampling clock as the reference, hence achieving better precision at higher sampling rates.

A programmable-gain AFE accurately controls the amplitude of the received signals. This AFE further helps reduce complexity and maintain linearity to achieve accurate fine detection. Without gain control, the envelop detection would have the same walk error problem as a pulsed lidar. If the walk error of the coarse detection exceeds the detection range of the fine detection (one cycle of the 19-GHz reference clock), the segmented detection would no longer be possible. The proposed solution uses a digitally automatic gain control (AGC) loop to adjust the gain of the AFE. A dual-threshold over-range detection of the ADC senses whether the signal is over-range or under-range and keeps the timing error of detecting the envelope less than a quarter cycle.

Tuning the gain of the amplifiers inevitably introduces the phase shift; therefore, it is important to reduce the cost of the gain tuning with amplifiers that are phase-invariant. Since the phase shift is proportional to the operating frequency [44], it is more difficult to maintain phase invariance at high carrier frequencies. Down-converting and segmenting the gain tuning ease the amplifier's design. The gain tuning is partitioned into the coarse and the fine stages. This arrangement lowers the occupied area, power consumption, and phase variation. The receiver takes a lower frequency clock as the reference input and uses a local PLL to generate the LO for the down-conversion mixer.

E. Frequency Planning

The homodyne down-conversion architecture in [43] uses a simple LO generation that only uses dividers and a mixer to minimize the clock jitter. The performance based on the coherent detection, however, is limited by several factors.

1) The crosstalk between the reference clock and the echoed signal at the same frequency lowers the sensitivity and the linearity. Specifically, the reference leaks to the incoming signal path, hence introducing an in-band spur. At the same time, the received signals with different power pull the clock phase and cause input-dependent phase shifts.
2) I/Q IF channels and two high-speed ADCs are required to reconstruct the mask's envelope leading to high power consumption. Additionally, the I/Q mismatch calibration process must be done before the normal acquisition.

In this heterodyne architecture, a local PLL synthesizes the LO to suppress the in-band reference leakage and crosstalk. A two-step down-conversion with digital down-mixing is implemented which improves the power efficiency and immunity to PVT variation without additional calibration. The choice of the LO frequency and ADC sampling depends on the signal bandwidth. Since the signal is composed of a carrier frequency at 19 GHz, a 148-MHz modulation, and the third-order harmonic of the modulation, the AFE requires a bandwidth of 1 GHz. To satisfy this requirement, the ADC is chosen to operate at higher than 2 GHz to avoid aliasing. An external divide-by-8 divider (HMC862A) provides a 2.375-GHz reference (CK_{in}) to the local PLL and the ADC.

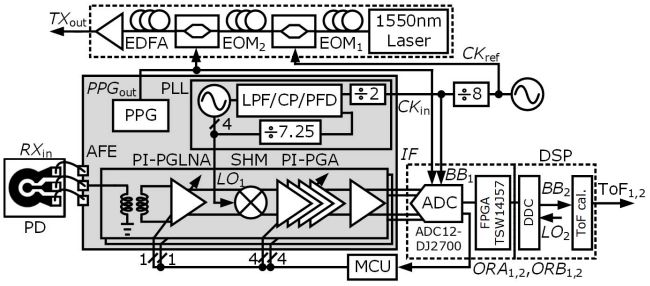

Fig. 9. Receiver implementation.

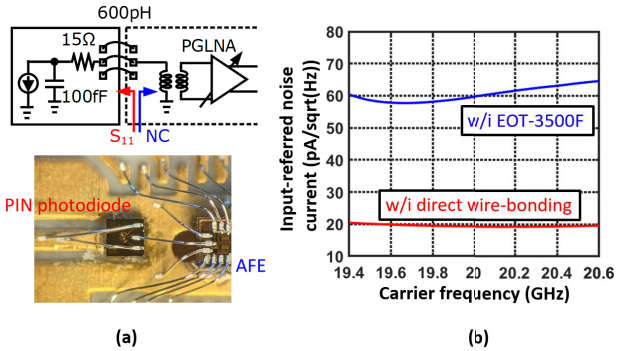

Fig. 10. Narrowband matching. (a) Schematic and wire-bonding photograph. (b) Input-referred noise current.

We set the IF frequency (f_{IF}) at 1.78 GHz ($3/32 f_{\mathrm{ref}}$), which is centered between the ADC sampling clock and its Nyquist rate, to obtain the maximum available bandwidth of 1 GHz. We then can derive the LO frequency (f_{LO1}) based on the RF frequency of 19 GHz and the IF frequency of 1.78 GHz, which is 17.2 GHz ($29/32 f_{\mathrm{ref}}$).

III. Receiver Implementation

Details of the receiver design are shown in Fig. 9. A high-speed p-i-n photodiode converts the echoed optical signal to an electrical RF signal. A 1-bit phase-invariant programmable-gain low-noise amplifier (PI-PGLNA) [42] and a 2× sub-harmonic mixer (SHM) with transimpedance amplifier (TIA) load [45] amplify and down-convert the RF signal into IF. A chain of phase-invariant programmable-gain amplifiers (PI-PGAs) with 4-bits of tuning covering a 50-dB gain range amplifies the IF signal and is followed by a subsampling ADC. The ADC employs dual-threshold over-range detection, ORA and ORB, to adjust the gain in a feedback loop to handle a wide range of input power. A DSP digitally down-converts (DDC) the captured data with a digital complex LO ($f_{\mathrm{LO2}} = 1/32 f_{\mathrm{ref}}$) to calculate the segmented and overall ToF.

A. AFE Design

To receive the narrowband signal, a photodiode is included in the design of the matching network. Fig. 10(a) shows the schematic and the photograph of the design. A 20-μm photodiode bare die is directly wire bonding to our AFE chip, and the 600-pH bond-wire acts as a matching network. The narrowband matching reduces the input-referred noise current by 2× compared to using an off-the-shelf photodiode module (EOT-3500F) with an internal 50-Ω termination. The simulation results of the noise performance are shown in Fig. 10(b) where the input-referred noise current density is 19 pA/$\sqrt{\mathrm{Hz}}$ with direct wire bonding and 60 pA/$\sqrt{\mathrm{Hz}}$ with EOT-3500F.

The proposed PI-PGA design is shown in Fig. 11(a). An inverter-based design is chosen for better linearity and smaller area when compared to using current mode logic (CML) in [42]. The unit cell of the PGA is an inverter with a control signal that enables it. The PGA can be viewed as a transconductance (G_m) with a load structure (R_l).

A current-steering transconductance keeps the input and output impedances constant for varying gain settings to minimize phase variation. The amplifier achieves the maximum gain when all forward units are turned ON and the equivalent G_m is g_{m1}. To reduce the gain of the amplifier, we turn off some units (α) in the forward path, and at the same time, turn on the same amount of the unit cells in the cross-coupled forward path. The conducting currents from both paths are subtracted at the output node, thus reducing the effective transconductance. The equivalent G_m of the phase-invariant amplifier is

$$G_m = g_{m1}(1 - 2\alpha). \tag{15}$$

The total number of inverters that are ON remains the same across different gain settings. With the fixed number of ON-units, the input and output impedances have a small variation across the gain tuning range.

The gain tuning range and the relative phase shift are shown in Fig. 11(b). The four-stage PGA achieves a 50-dB gain tuning range with only 2.8° relative phase shift. An additional phase-compensation unit is added to further compensate for the variation caused by the change of the Miller capacitance in the forward path and the cross-coupled forward path. When we turn ON the cross-coupled forward inverters, we also enable the same amount of units in the compensation branch. After compensating for the difference of the Miller capacitance, the relative phase shift is further reduced to within 0.7°.

The amplifier's load design is realized by cross-coupled inverters ($g_{m4,6}$) and diode-connected inverters ($g_{m5,7}$). This implementation decouples the common-mode gain and the differential-mode gain [46] by 48 dB as shown in Fig. 11(c). The decoupling of the common-mode gain and the differential-mode gain enables one-stage active feedback. Without the common-mode gain suppression, the load would form an unstable positive feedback loop in common mode. The active feedback loop with g_{m2} and g_{m3} extends the bandwidth, and the gain can be expressed as

$$g_{m1}(1 - 2\alpha)\frac{g_{m2} R_{l1,\mathrm{diff}} R_{l2,\mathrm{diff}}}{1 + g_{m2} g_{m3} R_{l1,\mathrm{diff}} R_{l2,\mathrm{diff}}} \tag{16}$$

where

$$R_{l1,2,\mathrm{diff}} = \frac{1}{g_{m5,7}} /\!/ \frac{-1}{g_{m4,6}}. \tag{17}$$

The closed-loop gain is approximately $g_{m1}(1 - 2\alpha)/g_{m3}$. In comparison to a TIA load, the active feedback load provides

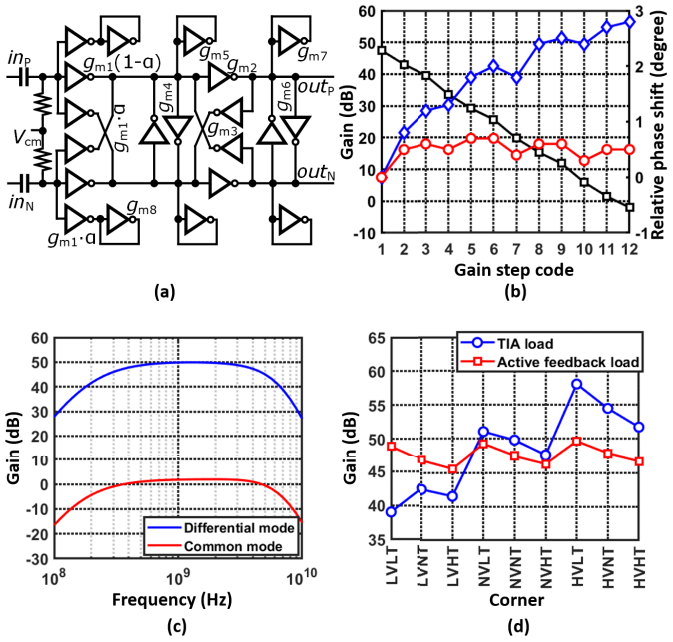

Fig. 11. (a) PI-PGA design. (b) Gain tuning range and relative phase shift. (c) Frequency response. (d) Gain variation in corners.

better immunity to PVT variation since the gain only depends on the ratio of the transconductances g_{m1} and g_{m3}. Fig. 11(d) compares these two different structures in simulation. The gain variation with the active feedback load reduces from 20 to 5 dB across -20 °C to 125 °C and $\pm 10\%$ supply variation.

B. LO Generation

The design goal of the PLL is to synthesize the 17.2-GHz LO frequency from the 2.375-GHz reference. There are two possible approaches as shown in Fig. 12(a) and (b). The design in Fig. 12(a) operates the PLL at full rate and the VCO operates at 17.2 GHz. The design in Fig. 12(a) uses a half-rate PLL operating at 8.6 GHz and uses an SHM to effectively double the LO frequency. This design chose the latter and operates the VCO at the half rate to prevent frequency pulling between the LO and the incoming signal. Furthermore, a ring-type VCO can be implemented at half rate, which enables a very small footprint and inherently provides multi-phase outputs. A key consideration of using a ring-type VCO in the PLL design is to properly filter the phase noise.

A conventional type-II PLL architecture is adopted in this design as shown in Fig. 12(c). With the design constraints of the input clock at 2.375 GHz and the output frequency at 8.6 GHz, various divide ratios of the feedforward divider (M and the feedback divider (N) are considered, which lead to different loop bandwidths. The impact of loop bandwidth on the output jitter can be seen in Fig. 12(d). Note that the reference noise is considered separately in our noise model (see Fig. 3). In an integer-N mode where $M = 8$ and $N = 29$, the jitter is dominated by the VCO. The jitter is reduced as the bandwidth increases (smaller divide ratio) but is eventually limited by the CP's noise. Considering the requirement of the VCO's phases and the performance, we select $M = 2$,

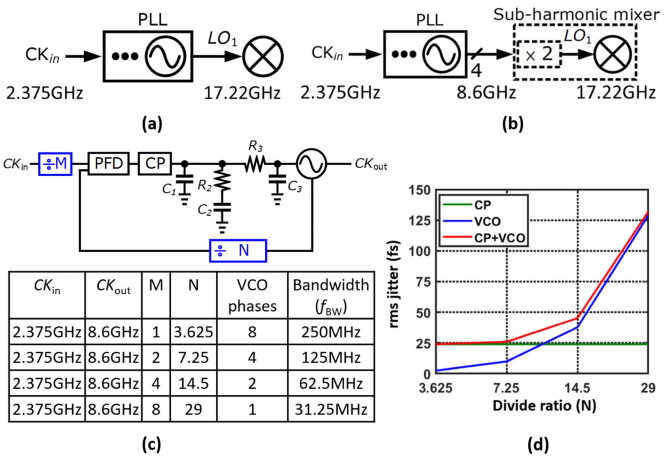

CK_{in}	CK_{out}	M	N	VCO phases	Bandwidth (f_{BW})
2.375GHz	8.6GHz	1	3.625	8	250MHz
2.375GHz	8.6GHz	2	7.25	4	125MHz
2.375GHz	8.6GHz	4	14.5	2	62.5MHz
2.375GHz	8.6GHz	8	29	1	31.25MHz

Fig. 12. LO generation. (a) Full-rate implementation. (b) Half-rate implementation. (c) Design choices. (d) RMS jitter.

$N = 7.25$, and the loop bandwidth of 100 MHz. The divide-by-7.25 divider and the SHM can be designed to share the same in-phase and quadrature-phase outputs from the VCO.

1) Ring-Type VCO Design: The proposed two-stage differential ring-type VCO and its delay cell are shown in Fig. 13(a). The elements are based on the clocked inverter in the standard cell library. The compact footprint of the standard cell reduces the area and the parasitics of the delay cell. The VCO's operating frequency is tuned by interpolating delays of the discrete-tuning path and the analog-tuning path. The hybrid frequency tuning covers a wide tuning range across the PVT variations and reduces the K_{VCO} to minimize the perturbation to the VCO.

In the discrete tuning path, the inverters with enable signal are controlled by a 3-bit digital word (en[2:0], enb[2:0]) which selects among eight-discrete bands to cover the process variation. In the analog-tuning path, the delay cell consists of parallel inverters in a cascade with transmission gates. The analog-tuning range is designed to accommodate the temperature (-20 °C to 125 °C) and supply variation ($\pm 10\%$) within a process corner. The transmission gates are designed such that all NMOSs are connected to the loop filter of the PLL. Half of the PMOSs are tied to HIGH (tieH), and the rest of the PMOSs are tied to LOW (tieL). The programmable connection to HIGH or LOW provides an additional tuning knob to linearize the frequency tuning curve. This VCO can operate from 5 to 12 GHz with eight discrete bands and a 1-GHz operating range for each discrete band [see Fig. 13(b)].

2) Divide-by-7.25 Fractional Divider: Fig. 14(a) shows the design of the divide-by-7.25 fractional divider, and Fig. 14(b) shows its timing diagram. The fractional divider consists of two 4-to-1 multiplexers with one-hot control, a divide-by-7 divider, a ring counter, and a re-timer. The inputs of the multiplexers are the four quadrature phases from the VCO. The operation starts by resetting the ring counter with one-hot output (S_{0-3}). Every seven input-clock cycles, the divide-by-7 divider (CK_c), triggers the ring counter, and the ring counter shifts one bit. The re-timer then senses the change of the ring counter, and its output (D_{0-3}) selects the next input phase of

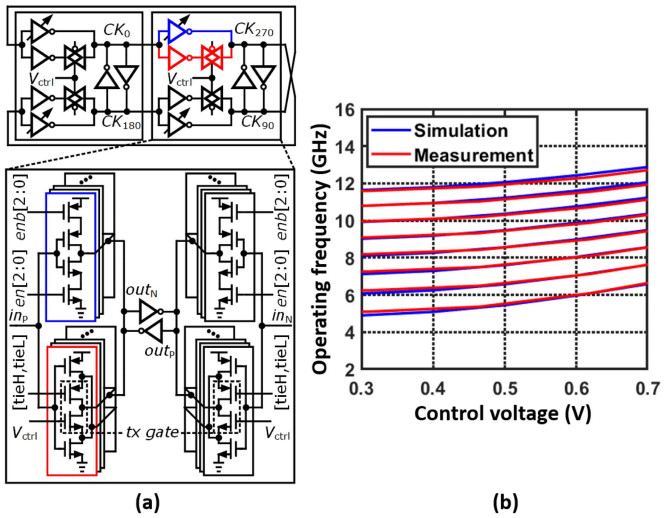

Fig. 13. (a) Ring-type VCO design and (b) frequency tuning range.

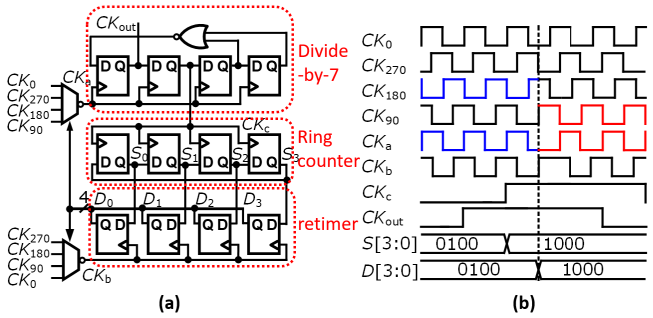

Fig. 14. (a) Divide-by-7.25 fractional divider design and (b) its timing diagram.

the 4-1 multiplexer. The selected input clock (CK_a) provides a 90° phase shift to the divider which leads to the fractional divider ratio. The four-input phases are matched carefully to reduce the fractional spur.

IV. Measurement Results

The die photograph of the DSP-based receiver is shown in Fig. 15. The receiver is fabricated in TSMC 28-nm CMOS technology with a 1.5 mm × 0.5 mm area, including the ESD bonding pad ring. The occupied active area is 0.39 mm^2 which includes two AFE channels, a shared local LO generator, and a synthesized digital logic block. At a 1-V supply, the total power consumption for two channels is 108 mW. Each AFE dissipates 36 mW per channel and the local PLL dissipates 36 mW including the LO driver.

Fig. 16(a) shows the measurement setup for characterizing the performance of the phase-invariant amplifiers. The phase-invariant amplifiers are characterized by a variable fiber optical attenuator (VOA). Compared to an electrical attenuator, the optical attenuator has a negligible impact on the phase of the RF carrier which mimics a realistic environment. The input power to the AFE is varied and the impact of the variation on the phase shift is measured. The measurement results of the PI-PGLNA and PI-PGA are shown in Fig. 16(b) and (c).

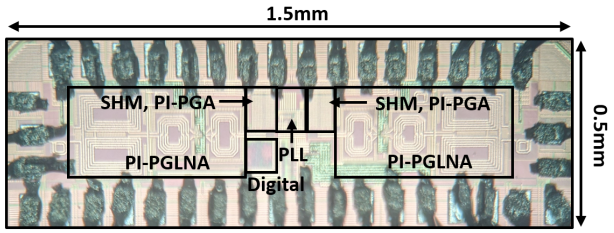

Fig. 15. Die photograph.

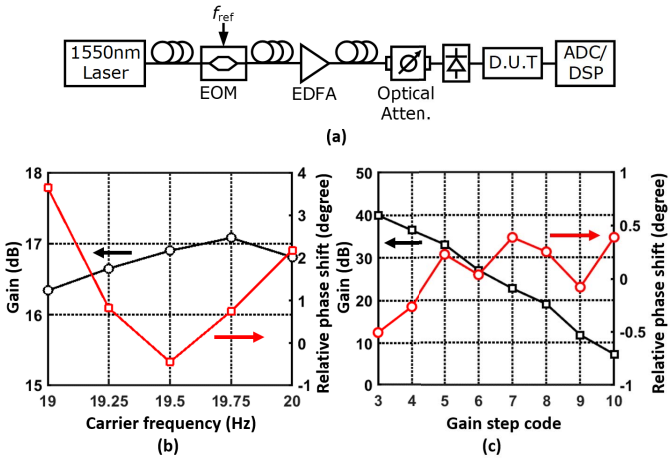

Fig. 16. Measurement results of the phase-invariant AFE. (a) Measurement setup. (b) PI-PGLNA. (c) PI-PGA.

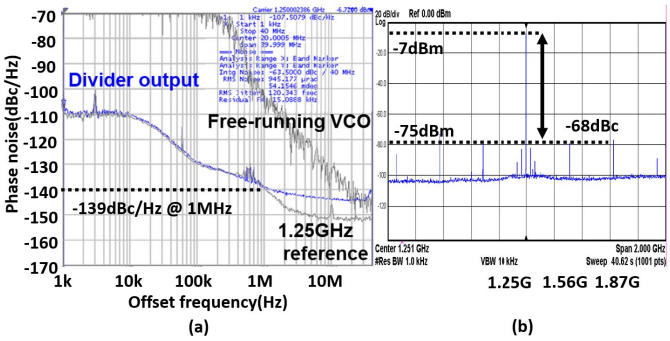

Fig. 17. Measurement results of PLL. (a) Phase noise. (b) Spectrum.

The PI-PGLNA achieves 17-dB gain tuning with 1-bit digital control centered at 19.5 GHz and less than 0.5° phase shift. The PI-PGA achieves a low phase variation of ±0.5° across the 40-dB gain range, which corresponds to ±10-μm accuracy.

The PLL phase noise measured at the divide-by-7.25 output (1.25 GHz) is shown in Fig. 17(a). The phase noise of the free-running VCO and the 1.25-GHz reference clock is also shown in the plot. The rms jitter of the PLL is 120 fs integrated from 1 kHz to 40 MHz. Fig. 17(b) shows the spectrum of the clock output at 1.25 GHz. The fractional spurs are −70 and −68 dBc at 312.5- and 625-MHz offset frequency. The second-order harmonic of the fractional spur causes in-band leakage and is the primary limitation of the receiver's sensitivity. The sensitivity of the receiver is −65 dBm without

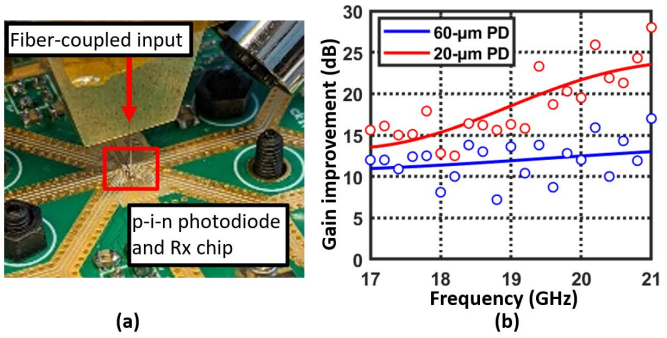

Fig. 18. Measurement results of direct wire-bonding. (a) Measurement setup. (b) Gain improvement comparing to the baseline design.

leakage cancellation. The leakage cancellation can be implemented in the DSP to further improve the sensitivity.

To verify the impact of photodiode area and narrowband matching, two different p-i-n photodiodes are used: a 20-μm photodiode (GCS Do231_20μm_C3 with responsivity = 0.75 A/W, C_{pd} = 80 fF) and a 60-μm photodiode (Phograin xsj-10-d5-60 with responsivity = 1.12 A/W, C_{pd} = 210 fF). We compare the narrowband approach to a baseline setup which is a fiber-coupled photodiode module with an internal 50-Ω termination (EOT-3500F). The measurement setup is shown in Fig. 18(a). The photodiodes are directly received from an EDFA via fiber. Fig. 18(b) shows the gain response of the two different photodiodes relative to the baseline. The measurement results validate the bandwidth extension and gain enhancement of the passive narrowband matching network.

To verify the receiver performance in a calibrated optical environment, the response to distance scanning (1-D) over free space is measured. The setup, as shown in Fig. 19(a), characterizes precision and linearity. A mirror target on a motorized stage (Aerotech ALS130-150) that is driven by an encoder is placed 2.5-m away from the transceiver. The emitted power of the transmitter is 6 dBm for the EoT-3500F and 0 dBm for the direct wire bonding. A circulator isolates the emitted and the returned laser beams. Fig. 19(b) and (c) shows the INL and the precision of the 1-D scanning. The maximum INL is 30 μm with the rms error of 13 μm. The mean of the precision across the 10-cm dynamic range with a 5-MSa/s sampling rate is 6.25 μm for the photodiode module with broadband termination, 6.28 μm for the 20-μm photodiode with direct wire-bonding, and 7.1 μm for the 60-μm photodiode with direct wire-bonding. It is worthwhile to note that the 2.5-m displacement and the 10-cm dynamic range are not limited by the transceiver itself but by the laboratory space and the stage's maximum operating range. Since the aperture of the fiber is less than 20 μm, the input power is constant for both p-i-n photodiodes. The measurement results verify the discussion in Section II-C that a small photodiode is favored for high precision if view-of-angle is not a concern.

To evaluate the response to a realistic target, Fig. 20(a) shows the setup for 2-D scanning with an MEMS mirror. To improve the optical isolation of the transmitter and the receiver, a polarizing beam splitter is inserted between the

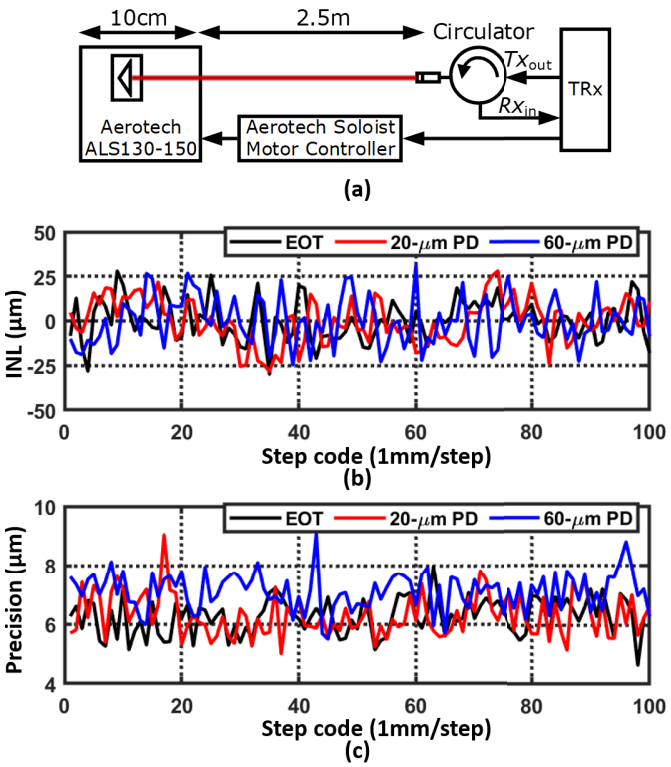

Fig. 19. (a) One-dimensional scanning setup, (b) linearity, and (c) precision, with different photodiode arrangements: 1) EOT-3500F with 6-dBm P_{tx}; 2) direct wire-bonding 20-μm photodiode with 0-dBm P_{tx}; and 3) direct wire-bonding 60-μm photodiode with 0-dBm P_{tx}.

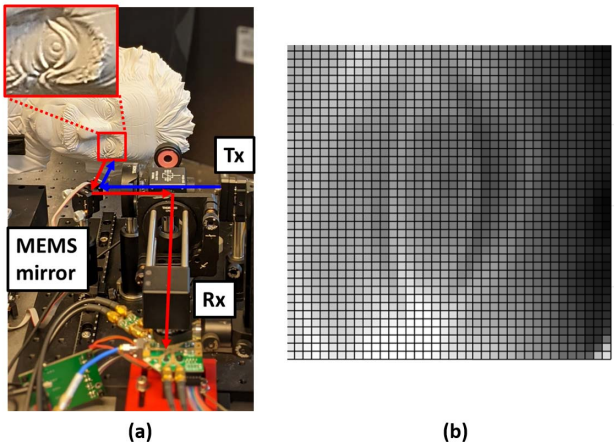

Fig. 20. Measurement results of 2-D scanning. (a) Measurement setup. (b) Scanning result.

transmitter, the MEMS mirror, and the receiver. The MEMS mirror from MirrorcleTech has a 5-mm diameter and a scanning angle of $\pm 5°$ in both X- and Y-directions. In this experiment, we use the 60-μm photodiode for a wider scanning angle and depth-of-view. A 3-D printed bust of Einstein is the target. The partial scanned result is shown in Fig. 20(b).

Table I summarizes the performance of the receiver and compares this work to the state-of-the-art lidar systems. The AFE achieves -65-dBm sensitivity with a 60-dB gain tuning range with only $\pm 0.5°$ relative phase shift. The ring-type VCO

TABLE I
SUMMARY TABLE

	ISSCC 2016 [14]	JSSC 2019 [13]	SSC-L 2020 [43]	TIM 2021 [8]	This work	
Architecture	FMCW	Pulsed	Pulsed-coherent	AMCW	Pulsed-coherent	
Technology	180nm CMOS 250nm Si-ph	110nm CIS	28nm CMOS	N/A	28nm CMOS	
Wavelength	1550nm	473nm	1590nm	1531nm 1534nm	1550nm	
PD Termination	Broadband	Broadband	Broadband	Broadband	Broadband	Narrowband
Emitted Power (P_{Tx})	10dBm	-5dBm	6dBm	−3dBm	6dBm	0dBm
$Range_{Max}$	1.4m	16cm	2.5m	5m	2.5m	
INL_{Max}	N/A	230μm	100μm	38μm	30μm	
Displacement (D)	5cm	14.75cm	250cm	500cm	250cm	
Dynamic range	0.1cm	2.5cm	10cm	0.03cm	10cm	
Depth Precision (σ)	8μm	64μm	9μm	19.2μm	6μm	6.6μm
Sampling rate (f_{Sa}) (Per Pixel)	180kHz	25Hz	5MHz	64kHz	5MHz	5MHz
FoM (dB-J)	−148	−117	−200	−189	−203	−209

has a wide operating range from 5 to 12.5 GHz with 120-fs rms jitter integrated from 1-kHz to 40-MHz offset frequency. This DSP-based pulsed-coherent lidar system achieves the maximum INL of 30 μm and the precision of 6 μm with 5-MHz integration bandwidth across a 10-cm dynamic range at 2.5-m displacement.

A figure-of-merit (FoM) [43]

$$\text{FoM} = 10\log\left[\left(\frac{P_{\text{Tx}}}{D^2}\right)\left(\frac{\sigma^2}{f_{\text{Sa}}}\right)\right] \tag{18}$$

is used to help comparing receivers including the photodetector and the electrical readout circuit, where P_{Tx}/D^2 indicates the received optical power (P_{Tx} is the transmitted optical power and D is the displacement), σ is the precision, and f_{Sa} is the sampling rate. Since the received optical power is not often provided directly in prior publications, we derive the received optical power from the emitted power, displacement, and assuming optimal path loss. We believe it is reasonable since, in the comparison table, all published results use a mirror as the target to characterize the depth precision. Our receiver achieves a low FoM of −203 dB-J with broadband photodiode termination and −209 dB-J with narrowband termination.

V. CONCLUSION

This work presents a pulsed-coherent lidar system that achieves high linearity and sub-10-μm depth precision with a 5-MHz sampling rate. The receiver has been implemented to enhance the robustness of the system to the environment. The noise analysis of the phase detection allows us to understand the design choices, such as the carrier frequency, the dimension of the photodiode, and the ADC requirement. We also develop the narrowband matching network to leverage the coherent nature of the approach and improve the sensitivity and efficiency of the receiver.

A discrete-tuning inverter-based programmable gain amplifier has been implemented. The phase-invariant AFE achieves less than 1° phase shift. In addition, a type-II PLL using a ring-type VCO has been used to minimize the noise contribution from the additive noise. We also integrate the electrical receiver with an optical transmitter and perform both 1-D and 2-D scanning for the system integration. With the precision and high sampling rate, this system can enhance the capability of current lidars and potentially enable new applications.

ACKNOWLEDGMENT

The authors would like to thank TSMC, Hsinchu, Taiwan, and the High Speed Electronics Laboratory, UCLA, Los Angeles, CA, USA, for fabrication support.

REFERENCES

[1] J. Pehkonen, P. Palojarvi, and J. Kostamovaara, "Receiver channel with resonance-based timing detection for a laser range finder," *IEEE Trans. Circuits Syst. I, Reg. Papers*, vol. 53, no. 3, pp. 569–577, Mar. 2006.

[2] S. Kurtti and J. Kostamovaara, "Laser radar receiver channel with timing detector based on front end unipolar-to-bipolar pulse shaping," *IEEE J. Solid-State Circuits*, vol. 44, no. 3, pp. 835–847, Mar. 2009.

[3] J. Nissinen, I. Nissinen, and J. Kostamovaara, "Integrated receiver including both receiver channel and TDC for a pulsed time-of-flight laser rangefinder with cm-level accuracy," *IEEE J. Solid-State Circuits*, vol. 44, no. 5, pp. 1486–1497, May 2009.

[4] C. Niclass, M. Soga, H. Matsubara, S. Kato, and M. Kagami, "A 100-m range 10-frame/s 340 × 96-pixel time-of-flight depth sensor in 0.18-μm CMOS," *IEEE J. Solid-State Circuits*, vol. 48, no. 2, pp. 559–572, Feb. 2013.

[5] F. Villa *et al.*, "CMOS imager with 1024 SPADs and TDCs for single-photon timing and 3-D time-of-flight," *IEEE J. Sel. Topics Quantum Electron.*, vol. 20, no. 6, pp. 364–373, Nov. 2014.

[6] M. Perenzoni, D. Perenzoni, and D. Stoppa, "A 64 × 64-pixels digital silicon photomultiplier direct tof sensor with 100-MPhotons/s/pixel background rejection and imaging/altimeter mode with 0.14% precision up to 6 km for spacecraft navigation and landing," *IEEE J. Solid-State Circuits*, vol. 52, no. 1, pp. 151–160, Jan. 2017.

[7] A. R. Ximenes, P. Padmanabhan, M.-J. Lee, Y. Yamashita, D. N. Yaung, and E. Charbon, "A 256×256 45/65 nm 3D-stacked spad-based direct TOF image sensor for LiDAR applications with optical polar modulation for up to 18.6 dB interference suppression," in *IEEE Int. Solid-State Circuits Conf. (ISSCC) Dig. Tech. Papers*, 2018, pp. 96–98.

[8] C. Zhang, Z. Zhang, Y. Tian, S. Y. Set, and S. Yamashita, "Comprehensive ranging disambiguation for amplitude-modulated continuous-wave laser scanner with focusing optics," *IEEE Trans. Instrum. Meas.*, vol. 70, pp. 1–11, 2021.

[9] C. Zhang, S. Y. Set, and S. Yamashita, "Enhancement in dynamic range of amplitude-modulated continuous-wave laser scanner having a coaxial configuration," *IEEE Trans. Instrum. Meas.*, vol. 70, pp. 1–10, 2021.

[10] Y.-S. Jang, J. Park, and J. Jin, "Sub-100-nm precision distance measurement by means of all-fiber photonic microwave mixing," *Opt. Exp.*, vol. 29, no. 8, pp. 12229–12239, Apr. 2021. [Online]. Available: http://www.opticsexpress.org/abstract.cfm?URI=oe-29-8-12229

[11] S. Zhang, Z. Xu, B. Chen, L. Yan, and J. Xie, "Sinusoidal phase modulating absolute distance measurement interferometer combining frequency-sweeping and multi-wavelength interferometry," *Opt. Exp.*, vol. 26, no. 7, pp. 9273–9284, Apr. 2018. [Online]. Available: http://www.opticsexpress.org/abstract.cfm?URI=oe-26-7-9273

[12] Z. Zhu, G. Xu, K. Ni, Q. Zhou, and G. Wu, "Synthetic-wavelength-based dual-comb interferometry for fast and precise absolute distance measurement," *Opt. Exp.*, vol. 26, no. 5, pp. 5747–5757, Mar. 2018. [Online]. Available: http://www.opticsexpress.org/abstract.cfm?URI=oe-26-5-5747

[13] K. Yasutomi, Y. Okura, K. Kagawa, and S. Kawahito, "A sub-100 μm-range-resolution time-of-flight range image sensor with three-tap lock-in pixels, non-overlapping gate clock, and reference plane sampling," *IEEE J. Solid-State Circuits*, vol. 54, no. 8, pp. 2291–2303, Aug. 2019.

[14] B. Behroozpour *et al.*, "11.8 chip-scale electro-optical 3D FMCW LiDAR with 8 μm ranging precision," in *IEEE Int. Solid-State Circuits Conf. (ISSCC) Dig. Tech. Papers*, Jan. 2016, pp. 214–216.

[15] T. Peltola, T. Ruotsalainen, P. Palojarvi, and J. Kostamovaara, "A receiver channel with a leading edge timing discriminator for a pulsed time-of-flight laser radar," in *Proc. 26th Eur. Solid-State Circuits Conf.*, 2000, pp. 427–430.

[16] T. Ruotsalainen, P. Palojarvi, and J. Kostamovaara, "A wide dynamic range receiver channel for a pulsed time-of-flight laser radar," *IEEE J. Solid-State Circuits*, vol. 36, no. 8, pp. 1228–1238, Aug. 2001.

[17] S. Kurtti and J. Kostamovaara, "An integrated optical receiver with wide-range timing discrimination characteristics," in *Proc. 31st Eur. Solid-State Circuits Conf. (ESSCIRC)*, 2005, pp. 435–438.

[18] S. Petitgrand, R. Yahiaoui, K. Danaie, A. Bosseboeuf, and J. Gilles, "3D measurement of micromechanical devices vibration mode shapes with a stroboscopic interferometric microscope," *Opt. Lasers Eng.*, vol. 36, no. 2, pp. 77–101, 2001. [Online]. Available: https://www.sciencedirect.com/science/article/pii/S0143816601000409

[19] Y.-S. Jang, K. Lee, S. Han, J. Lee, Y.-J. Kim, and S.-W. Kim, "Absolute distance measurement with extension of nonambiguity range using the frequency comb of a femtosecond laser," *Opt. Eng.*, vol. 53, no. 12, pp. 1–6, 2014, doi: 10.1117/1.OE.53.12.122403.

[20] N. R. Doloca, K. Meiners-Hagen, M. Wedde, F. Pollinger, and A. Abou-Zeid, "Absolute distance measurement system using a femtosecond laser as a modulator," *Meas. Sci. Technol.*, vol. 21, no. 11, Sep. 2010, Art no. 115302, doi: 10.1088/0957-0233/21/11/115302.

[21] H. J. Kang, B. J. Chun, Y.-S. Jang, Y.-J. Kim, and S.-W. Kim, "Real-time compensation of the refractive index of air in distance measurement," *Opt. Exp.*, vol. 23, no. 20, pp. 26377–26385, Oct. 2015. [Online]. Available: http://www.opticsexpress.org/abstract.cfm?URI=oe-23-20-26377

[22] K.-N. Joo, Y. Kim, and S.-W. Kim, "Distance measurements by combined method based on a femtosecond pulse laser," *Opt. Exp.*, vol. 16, no. 24, pp. 19799–19806, Nov. 2008. [Online]. Available: http://www.opticsexpress.org/abstract.cfm?URI=oe-16-24-19799

[23] D. Onori, F. Laghezza, F. Scotti, M. Scaffardi, and A. Bogoni, "Coherent radar/LiDAR integrated architecture," in *Proc. Eur. Radar Conf. (EuRAD)*, Sep. 2015, pp. 241–244.

[24] M. D. Adams, "Coaxial range measurement–current trends for mobile robotic applications," *IEEE Sensors J.*, vol. 2, no. 1, pp. 2–13, Aug. 2002.

[25] C. S. Bamji *et al.*, "A 0.13 μm CMOS system-on-chip for a 512 $\times$ 424 time-of-flight image sensor with multi-frequency photo-demodulation up to 130 MHz and 2 GS/s ADC," *IEEE J. Solid-State Circuits*, vol. 50, no. 1, pp. 303–319, Jan. 2015.

[26] C. Zhang, S. Liu, Z. Zhang, L. Jin, S. Y. Set, and S. Yamashita, "Amplitude-modulated continuous-wave light detection and ranging with Bessel beamforming," in *Proc. Conf. Lasers Electro-Opt.*, 2020, pp. 1–2.

[27] A. Leven, V. Hurm, R. Reuter, and J. Rosenzweig, "Design of narrow-band photoreceivers by means of the photodiode intrinsic conductance," *IEEE Trans. Microw. Theory Techn.*, vol. 49, no. 10, pp. 1908–1913, Oct. 2001.

[28] C. E. Kacou, J. L. Polleux, M. Villegas, G. Chrétien, and A. LeBorgne, "Design of a low noise TIA between 4.4 and 5 GHz for RoF applications on a GaAs phemt technology," in *Proc. 13th Medit. Microw. Symp. (MMS)*, 2013, pp. 1–4.

[29] S. D. Greaves and R. T. Unwin, "The design of tuned front-end GaAs MMIC optical receivers," *IEEE Trans. Microw. Theory Techn.*, vol. 44, no. 4, pp. 591–597, Apr. 1996.

[30] P. Xiao and Z. Wang, "5.2 GHz CMOS narrow-band optical receiver for radio-over-fiber," in *Proc. Int. Conf. Commun., Circuits Syst.*, Jun. 2006, pp. 1937–1941.

[31] L. Bogaert *et al.*, "Narrowband photoreceiver for analog radio-over-fiber in the 24.25–29.5 GHz band," in *Proc. 45th Eur. Conf. Opt. Commun. (ECOC)*, 2019, pp. 1–4.

[32] L. Bogaert *et al.*, "36 Gb/s narrowband photoreceiver for mmWave analog radio-over-fiber," *J. Lightw. Technol.*, vol. 38, no. 12, pp. 3289–3295, Jun. 15, 2020.

[33] Y. Baeyens *et al.*, "Millimeter-wave long-wavelength integrated optical receivers grown on GaAs," *IEEE Photon. Technol. Lett.*, vol. 11, no. 7, pp. 868–870, Jul. 1999.

[34] L. Gomez-Rojas, N. J. Gomes, X. Wang, P. A. Davies, and D. Wake, "High performance optical receiver using a pin photodiode and amplifier for operation in the millimeter-wave region," in *Proc. 30th Eur. Microw. Conf.*, 2000, pp. 1–3.

[35] T. J. Kippenberg, R. Holzwarth, and S. A. Diddams, "Microresonator-based optical frequency combs," *Science*, vol. 332, no. 6029, pp. 555–559, Jun. 2011.

[36] S.-W. Huang *et al.*, "Mode-locked ultrashort pulse generation from on-chip normal dispersion microresonators," *Phys. Rev. Lett.*, vol. 114, Feb. 2015, Art no. 53901, doi: doi/10.1103/PhysRevLett.114.053901.

[37] B. Stern, X. Ji, Y. Okawachi, A. L. Gaeta, and M. Lipson, "Battery-operated integrated frequency comb generator," *Nature*, vol. 562, pp. 401–405, 2018.

[38] N. Picqué and T. W. Hänsch, "Frequency comb spectroscopy," *Nature Photon.*, vol. 13, no. 3, pp. 146–157, 2019.

[39] P. Trocha *et al.*, "Ultrafast optical ranging using microresonator soliton frequency combs," *Science*, vol. 359, no. 6378, pp. 887–891, Feb. 2018.

[40] J. Riemensberger *et al.*, "Massively parallel coherent laser ranging using a soliton microcomb," *Nature*, vol. 581, no. 7807, pp. 164–170, May 2020.

[41] Z. Zang, Z. Li, Y. Luo, Y. Han, X. Liu, and H. Y. Fu, "Ultrafast parallel LiDAR with time-encoding and spectral scanning: Breaking the time-of-flight limit," 2021, *arXiv:2103.05360*.

[42] L.-Y. Chen and C.-K.-K. Yang, "A 19-GHz pulsed-coherent ToF receiver with 40-μm precision for laser ranging systems," in *Proc. IEEE 45th Eur. Solid State Circuits Conf. (ESSCIRC)*, Sep. 2019, pp. 191–194.

[43] L.-Y. Chen, A. K. Vinod, J. Mcmillan, C. W. Wong, and C.-K.-K. Yang, "A 9-μm precision 5-MSa/s pulsed-coherent LiDAR system with sub-sampling receiver," *IEEE Solid-State Circuits Lett.*, vol. 3, pp. 262–265, 2020.

[44] F. Ellinger, U. Jorges, U. Mayer, and R. Eickhoff, "Analysis and compensation of phase variations versus gain in amplifiers verified by SiGe HBT cascode RFIC," *IEEE Trans. Microw. Theory Techn.*, vol. 57, no. 8, pp. 1885–1894, Aug. 2009.

[45] R. M. Kodkani and L. E. Larson, "A 24-GHz CMOS passive subharmonic mixer/downconverter for zero-if applications," *IEEE Trans. Microw. Theory Techn.*, vol. 56, no. 5, pp. 1247–1256, May 2008.

[46] B. Nauta, "A CMOS transconductance-C filter technique for very high frequencies," *IEEE J. Solid-State Circuits*, vol. 27, no. 2, pp. 142–153, Feb. 1992.

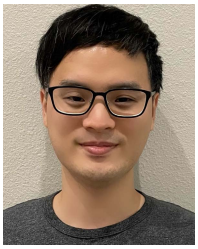

Li-Yang Chen (Member, IEEE) received the B.S. degree in physics from National Tsing Hua University, Hsinchu, Taiwan, in 2012, the M.S. degree from the Graduate Institute of Electronics Engineering, National Taiwan University, Taipei, Taiwan, in 2015, and the Ph.D. degree in electrical and computer engineering from the University of California at Los Angeles, Los Angeles, CA, USA, in 2021.

He is currently a Staff Analog/Mixed Signal Design Engineer with Xilinx, Inc., San Jose, CA, USA. His research interests include lidar/radar and high-speed wireline transceivers.

Abhinav Kumar Vinod received the B.S. degree from IIT Bombay, Mumbai, India, in 2014, and the M.S. and Ph.D. degrees from the University of California at Los Angeles, Los Angeles, CA, USA, in 2016 and 2021, respectively.

His research interests include optical frequency combs, ultrafast optics, 2-D materials, and quantum optics.

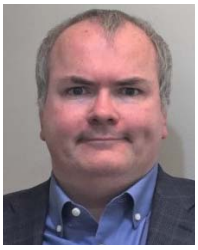

James F. McMillan received the B.A.Sc. degree from the University of Toronto, Toronto, ON, Canada, in 2004, and the M.S. and Ph.D. degrees from Columbia University, New York, NY, USA, in 2012 and 2019, respectively.

He is currently a Post-Doctoral Researcher with the Mesoscopic Optics and Quantum Electronics Laboratory, University of California at Los Angeles, Los Angeles, CA, USA.

Hangbo Yang received the B.S. degree in optical information science and technology from Wuhan University, Wuhan, Hubei, China, in 2012, and the Ph.D. degree in optical engineering from Zhejiang University, Hangzhou, Zhejiang, China, in 2017.

Since 2018, he has been a Post-Doctoral Researcher with the University of California at Los Angeles, Los Angeles, CA, USA. His research interests include waveguide display, front-end Fourier image processors, and LiDAR chips.

Chee Wei Wong (Fellow, IEEE) received the B.Sc. and B.A. degrees (Hons.) from the University of California at Berkeley, Berkeley, CA, USA, in 1996 and 1999, respectively, and the M.Sc. and D.Sc. degrees from the Massachusetts Institute of Technology, Cambridge, MA, USA, in 2001 and 2003, respectively.

He was a tenured Faculty Member with Columbia University, New York, NY, USA. He currently serves as a Faculty Member with the University of California at Los Angeles, Los Angeles, CA, USA.

Dr. Wong was elected as a member of the National Academy of Inventors, and a fellow of APS, OSA, ASME, and SPIE. He was a recipient of the NIH Early Scientist Trailblazer Award, the DARPA Young Faculty Award, the NSF CAREER Award, the Google Faculty Award, and 3M Faculty Award among others. He is also a finalist in the Qualcomm Innovation Award, the Maiman Award, and holds the visiting professorship at the Chinese Academy of Sciences and the Global Foundry visiting professorship at the National University of Singapore.

C.-K. Ken Yang (Fellow, IEEE) was born in Taipei, Taiwan. He received the B.S., M.S., and Ph.D. degrees in electrical engineering from Stanford University, Stanford, CA, USA, in 1992 and 1998, respectively.

In 1999, he joined the University of California at Los Angeles, Los Angeles, CA, USA, where he has been a Professor since 2009. His current research interests include high-performance mixed-mode circuit design for very-large-scale integration systems and include clock generation, high-performance signaling, low-power digital functional blocks, analog-to-digital conversion, high-voltage generation, and building blocks for computer networks.